Journal of ELECTRONIC MATERIALS, Vol. 49, No. 1, 2020
https://doi.org/10.1007/s11664-019-07708-3

Ultrasound-Assisted Method for Preparation of Ag_2S Nanostructures: Fabrication of Au/Ag_2S-PVA/n-Si Schottky Barrier Diode and Exploring Their Electrical Properties

Y. BADALI,[1] Y. AZIZIAN-KALANDARAGH,[2,3,7] EHSAN A. AKHLAGHI,[4,5] and Ş. ALTINDAL[6]

1.—Department of Advanced Technologies, Institute of Science and Technology, Gazi University, 06560 Ankara, Turkey. 2.—Department of Physics, University of Mohaghegh Ardabili, P.O. Box 179, Ardabil, Iran. 3.—Department of Engineering Sciences, Sabalan University of Advanced Technologies (SUAT), Namin, Iran. 4.—Department of Physics, Institute for Advanced Studies in Basic Sciences (IASBS), Zanjan 45137-66731, Iran. 5.—Optics Research Center, Institute for Advanced Studies in Basic Sciences (IASBS), Zanjan 45137-66731, Iran. 6.—Department of Physics, Faculty of Sciences, Gazi University, Ankara, Turkey. 7.—e-mail: yashar.a.k@gmail.com

Au/*n*-Si metal/semiconductor (MS) Schottky barrier diodes with and without (Ag_2S-PVA) interlayer were prepared by the ultrasound-assisted method and their electric and dielectric properties were examined by using current–voltage (*I*–*V*) and capacitance–voltage (*C*–*V*) measuring devices. The structural, optical and morphological characteristics of the (Ag_2S-PVA) were studied by x-ray diffraction (XRD), scanning electron microscopy (SEM) and UV–Visible spectroscopy. The observed peaks in the XRD pattern are related to the α-phase of silver sulfide. The UV–Visible spectrum of (Ag_2S-PVA) shows the quantum confinement and SEM image proves the grain size in nano-scale. The ideality factor (n) and barrier height (BH) at zero bias ($\Phi_{B0}(I–V)$) were acquired from the *I*–*V* data. On the other hand; Fermi energy (E_F), donor concentration atoms (N_D), and BH ($\Phi_B(C–V)$) values were obtained from the reverse bias *C*–*V* data. The voltage-dependent resistance profile ($Ln(R_i)–V$) was obtained by applying Ohm's law and also by the Nicollian–Brews methods. Also, considering the voltage-dependent n and BH, $N_{ss}–(E_c–E_{ss})$ profile was acquired from the forward biases *I*–*V* characteristics. Depending on high, intermediate and low biases ln(*I*)–Ln(*V*) curves have three linear regions with distinct slopes for MS and MPS structures. The predominant current-transport mechanisms were obtained in related regions via trap-charge limited current and space-charge limited current, respectively. These outcomes indicate that the (Ag_2S-PVA) interlayer enhanced the performance of the diode considerably in terms of high rectifier rate (RR), shunt resistance (R_{sh}), and low surface states (N_{ss}) and series resistance (R_s). Thus, the (Ag_2S-PVA) interlayer can be used in MS type diode instead of a traditional insulator layer.

Key words: Au/Ag2S-PVA/*n*-Si, Schottky barrier diode, surface states, ultrasound-assisted method

INTRODUCTION

In recent decades, nanomaterials that have a large surface area to volume ratio have become a more interesting issue for researchers due to their

(Received January 20, 2019; accepted October 9, 2019; published online November 12, 2019)

unique properties.[1–3] This large-surface area is more effective on the structural, optical and electrical properties of the materials.[4–6] The quantization effects are the main impact of nanometer-size on prepared materials due to the electrons movement confinement which causes discrete energy levels based on the size of the nanomaterials.[7–9] The nanostructures, which are building blocks for fabricating functional nanoscale systems in the technological applications such as nano-electronics nano-computing, biological and medical sensing,[10–12] have been extensively synthesized and their characterization has been investigated by researchers.

Silver sulfide (Ag_2S) is an effective I–VI semiconductor material which has direct-bandgap ($\sim$ 1–2 eV), high-absorption coefficient,[13,14] and three allotropic forms including α (monoclinic phase at room temperature), β (bcc phase between 180 °C and 600 °C), and γ (fcc phase up to 600 °C). The α-Ag_2S is a semiconductor with nearly a direct bandgap of 0.9–1.1 eV.[15,16] In addition, Ag_2S is widely used in active absorbents of radio waves,[17] superionic conductors,[18] photoconductive cells,[19] infrared detectors,[20] solar cells,[21] electrochemical storage cells,[22] magnetic field sensors,[23] and Schottky barrier diodes (SBDs).[24]

Usually, metal/semiconductor (MS) type SBDs consist of a semiconductor between two metal electrodes. When a natural or synthesis thin insulator (composite or polymer) layer is sandwiched between metal and semiconductor, the MS is converted to MIS or MPS type SBDs. Since these two materials (metal and semiconductor) make contact with each other under high vacuum and temperature, a potential barrier occurs at metal and semiconductor interface due to the diffusion of electronic charges (electron and holes) and then these electronics charges have to pass over this obstacle/barrier for current. High-frequency applications are utilized from SBDs on numerous occasions due to their proper high-speed switching specifications. While the predominant current-transport or conduction mechanism in SBDs depends on majority carriers, in *p–n* junction diodes depends on minority carriers especially at room temperatures and above. When MS and *p–n* type diodes are compared with each other, the switching speed of MS diodes is quite faster than *p–n* junction diodes. Also, while th device is on, MS diodes have a lower forward voltage drop (V_F) and lower overshooting voltage than p–n junction diodes.[25–28]

In the literature, there are diversified methods to make Ag_2S nanostructures such as gamma-irradiation,[29] microemulsion,[30] successive ionic layer adsorption and reaction (SILAR),[31] thermal evaporation,[32] hydro-thermal,[33] spray pyrolysis deposition (SPD),[34] sol–gel,[35] microwave-assisted[36] ultrasound-assisted,[37] gas–solid reaction approach,[38] bacterial synthesis[39] and template methods.[40] Among them; ultrasound-assisted technique comprises the precursor ultrasound irradiation during synthesis and it has marked some advantages; for example, it has good compositional control, low cost; it has low-temperature crystallization and it does not need much equipment. Ultrasound irradiation has been used extensively to generate new materials with attractive features. Due to the great physical and chemical results of ultrasonic waves in solution, by the use of this technique, we can fabricate new materials with attractive properties.[41,42]

In our previous works,[43–46] some polyvinyl alcohol (PVA)-doped nanostructures such as Cu_2O-PVA, ZnS-PVA, CuS-PVA, and SnO_2-PVA were synthesized and then used as an interface thin layer between metal and semiconductor to create MPS type SBDs. The obtained experimental results represented that the use of such an interlayer increased the performance of the MS type SBDs in the respect of lower values of surface states (N_{ss}) and series resistance (R_s) and higher rectifying rate (RR = I_F/I_R) for high enough forward and reverse bias voltages, shunt resistance (R_{sh}) and barrier height (BH). These interface layers prevented the inter-diffusion between metal and semiconductor and isolated them. In this study, the Ag_2S-PVA nanostructure was prepared by the ultrasound-assisted method and then this nanostructure was deposited in the Au/*n*-Si interface. The current–voltage (*I–V*) and capacitance–voltage (*C–V*) and conductance-voltage (G/ω–*V*) were utilized to uncover the electrical and also dielectric qualifications of the fabricated MS and MPS structure at room temperature. These qualifications determine the effect of Ag_2S-PVA on Au/*n*-Si performance and to understand whether we can use this polymer interlayer instead of a traditional insulator/oxide layer such as SiO_2, TiO_2, etc.

MATERIALS AND METHODS

Preparation of α-Ag_2S Nanostructures in the Presence of PVA

Silver nitrate ($AgNO_3$), ($Na_2S{\cdot}9H_2O$), Polyvinyl alcohol (PVA $(C_2H_4O)_x$) powder and pure ethanol purchased from Merck. Preparing 0.2 M solution, 0.68 g $AgNO_3$ and 0.96 g $Na_2S{\cdot}9H_2O$ were dissolved in 20 mL pure water. Following, 1 mL PVA (5%) was added to this solution and the black mixture was prepared. After that, high ultrasound-irradiation (200 W/cm^2, 24 kHz) was applied to this mixture under normal atmospheric conditions for 15 min using Dr. Hielscher ultrasonic devices. When the reaction was finalized, the sediments were centrifuged and washed with ethanol and distilled water 5 times and dried in air condition. The reactions take place as follows:

$$2AgNO_{3(aq)} + Na_2S_{(aq)} \rightarrow Ag_2S_{(s)} + 2NaNO_{3(aq)}. \quad (1)$$

Fabrication of Au/Ag_2S-PVA/*n*-Si Schottky Barrier Diode

The phosphors (P) doped single crystalline silicon wafer (*n*-Si) with (110) orientation, 300 μm thickness, and 0.2 Ωcm resistance was purchased from Sigma-Aldrich to fabricate the Ag_2S-PVA interlayered and without interlayered MS structures. At first, following cleaning with methanol, the silicon wafer was rinsed in de-ionized water for 1 h. After that, this silicon was etched in a hot solution of H_2O, NH_4OH, and H_2O_2 (65:13:13 v/v) and again rinsed in de-ionized water. In the last step of cleaning in the silicon wafer process, the *n*-Si wafer was etched in a solution of H_2O:HF (24:1 v/v) and once again de-ionized water was used for washing. After this cleaning process, immediately the silicon wafer was put in a high-vacuum ($\sim 1.33 \times 10^{-7}$ kPa) thermal deposition chamber and pure gold (99.99%) was used for deposition as a target metal. A thin film of Au with almost 1300 Å thickness was thermally evaporated via tungsten filament overall backside of the Si wafer. After that, the sample was annealed at 550 °C to obtain a low resistance ohmic contact. At the next stage, the prepared Ag_2S-PVA composite was coated on the forepart of the Si by the spin-coating process. Finally, the thermal evaporation system was used in the same way as in the ohmic contact to perform rectifier contact. In this process, the pure Au dots with 1 mm diameter and approximately 1300 Å thickness was deposited on the Ag_2S-PVA thin layer. Thus, the fabrications of Au/Ag_2S-PVA/*n*-Si (MPS) type SBD were completed. More information on the structural analysis of the Ag_2S-PVA interfacial layer, schematic diagram of the SBDs and the system of the admittance ($Y = 1/Z$), (C–V and G/ω–V) measurements can be seen in our previous study.[43–46]

RESULT AND DISCUSSION

Structural and Optical Properties

X-ray Diffraction (XRD)

Figure 1 indicates the XRD pattern of Ag_2S-PVA nanostructure. No additional peaks were observed due to the high purity of this material. All peaks of diffraction may be easily marked to the monoclinic (α phase) of Ag_2S (PDF file No. 00-014-0072).

The mean crystallite size of PVA capped α-Ag_2S nanostructures was obtained by the Debye–Scherrer equation:

$$D = 0.9\lambda/\beta\cos\theta. \quad (2)$$

As λ is the wavelength of CuKα and D is the symbol of the average crystallite size, the full width at half maximum of the diffraction peak of the nanostructure and the Bragg angle were denoted by β and θ, respectively, in this expression.[47] The calculated PVA capped α-Ag_2S nanocrystallite size is less than 34 nm.

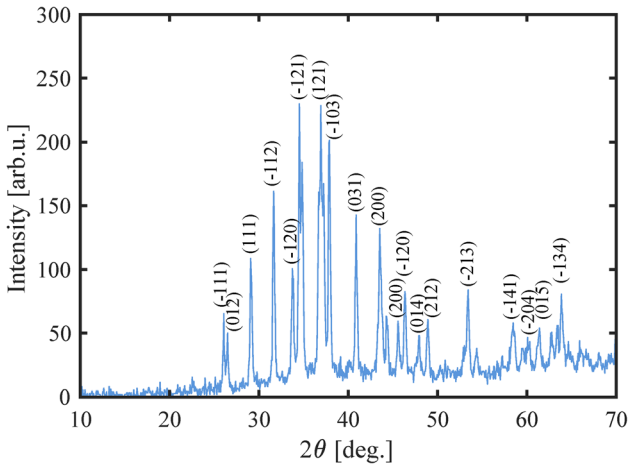

Fig. 1. XRD pattern of PVA capped α-Ag_2S nanostructure.

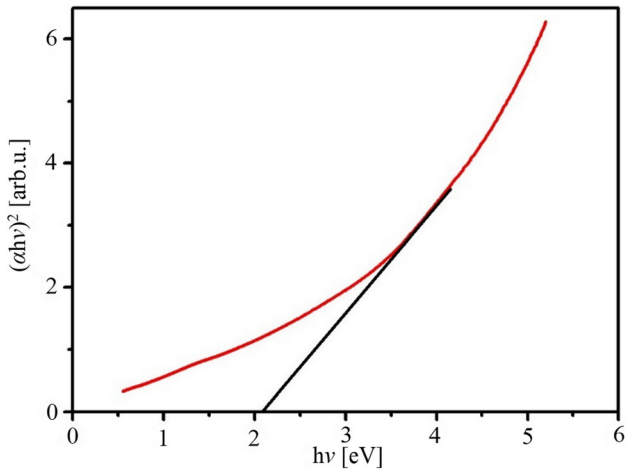

Fig. 2. Tauc curve of PVA capped Ag_2S nanostructure.

UV–Vis Analyses

Figure 2 indicates the Tauc curve of $(\alpha h\nu)^2$ versus $(h\nu)$ for Ag_2S-PVA nanostructure. The absorption bandgap energy (E_g) of the materials can be defined as follows:

$$(\alpha h\nu)^2 = A(h\nu - E_g). \quad (3)$$

In this expression, A is a constant and the photon energy and the absorption factor are denoted by $h\nu$ and α, respectively.[48] The corresponding bandgap energy for PVA capped α-Ag_2S was obtained as 2.1 eV. The little increase in the E_g may be related to the quantum confinement effect of the α-Ag_2S nanostructures.

Scanning Electron Microscopy (SEM)

Figure 3 shows the scanning electron microscopy (SEM) analysis of Ag_2S-PVA nanostructures obtained by the ultrasound-assisted method. The

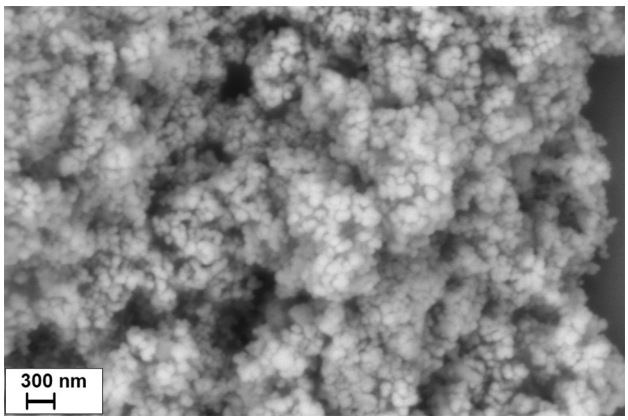

Fig. 3. SEM image of PVA capped Ag_2S nanostructure.

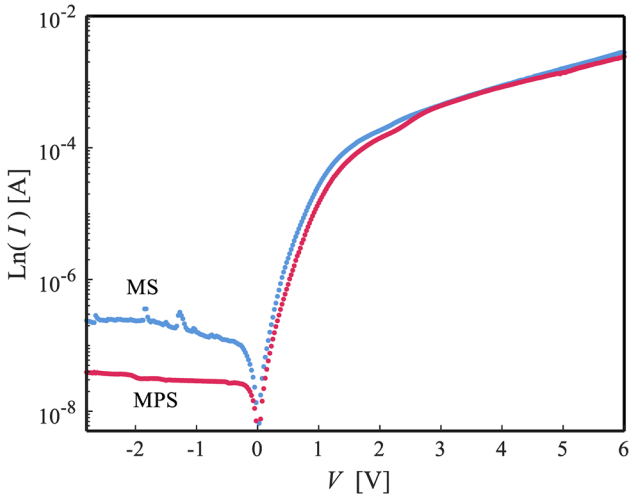

Fig. 4. The current–voltage (*I–V*) curves of the fabricated Au/*n*-Si (MS) and Au/(Ag_2S-PVA)/*n*-Si (MPS) SBDs.

SEM image shows the PVA capped Ag_2S nanostructures are in nanoscale and have a smooth spherical shape.

Electrical Characteristics

Current–Voltage (I–V) Characteristics

Figure 4 indicates the logarithmic *I–V* curves of the Au/*n*-Si (MS) SBDs with and without interfacial (Au/(Ag_2S-PVA)/*n*-Si) layer between − 3 V and + 6 V. As illustrated in Fig. 4, both the MS and MPS structure has a rectifying rate (RR= I_F/I_R at ± 3 V) but the RR value for MPS structure is 38 times higher than MS structure. In other words, the used (Ag_2S-PVA) interfacial layer leads to a considerable decline (38 times) in the value of leakage current due to its passivation effect on surface states (N_{ss}) and dislocations.

The basic electrical parameter of the MS and MPS structure was acquired from the intercept and slopes of the linear region of Ln(*I*) versus *V* via standard thermionic emission (TE) theory. To examine how close is the MPS structure to the ideal diode behavior, the experimental forward biases *I–V* properties of these structures at intermediate bias voltages ($V \geq 3\ kT/q$) were analyzed by using following relation[49–51]:

$$I = \underbrace{AA * T^2 \exp(-q\Phi_{Bo}/kT)}_{I_o} \left[\exp\left(\frac{q(V - IR_s)}{nkT}\right) - 1\right]. \quad (4)$$

In Eq. 4, the pre-factor used before the bracket is the reverse saturation current (I_0), Φ_{B0} is the zero-bias barrier height, *n* is the ideality factor, A^* is the Richardson constant (112 $A.cm^{-2}K^{-2}$ for *n*-Si), *A* is the rectifier contact area of the diode, and the (V_{Rs}= IR_s) is the voltage drop on the series resistance (R_s), respectively.[52] Thus, the values of I_0, *n*, and Φ_{B0} were found as 1.17×10^{-7} A, 6.78, and 0.74 eV for the MS and 3.62×10^{-8} A, 6.17, and 0.77 eV for the MPS structure, respectively. These results also confirmed the utilized (Ag_2S-PVA) interface layer causes the increase of MS type SBD performance. Moreover, as illustrated in Fig. 4, the current value in the forward biases exponentially increases with the increasing voltage and then deviation revealed due to the presence of the R_s and deposited interface layer. As implied in Fig. 4, in the reverse biases zone there is not a significant increase in current value when compared to the forward bias region. But, there is not any clear saturation in the forward bias region due to some reasons, for example; image force lowering of BH due to an external electric field, recombination current and the presence of the interface layer between metal and semiconductor.[53–55] Additionally, many surface states or traps can appear between metal and semiconductor which cause electronic states with energies located in the forbidden bandgap of the semiconductor. These traps lead to an increase in leakage current. But, the formation of barrier height between metal and semiconductor and its in-homogeneities are effective in the current transport mechanism, especially in the forward bias region.

The other two main electrical parameters are the shunt and series resistances (R_{sh} and R_s) of the diodes, which are more effective on the performance of electronic devices such as diodes, photodiodes, and solar cells. As R_s value is effective on the high forward biases, the influence of R_{sh} is evident in the reverse biases. There are various methods reported in the literature to determine the value of R_s such as Ohm's law,[49] Norde,[52] and Cheung's function.[56] Firstly, the voltage-dependent profile of resistance (R_i) was carried via Ohm's law (R_i= V_i/I_i) for both structures, which are represented in Fig. 5. Usually, the R_s values may be based on the ohmic contact, the contact manufactured by the probe wires to the rectifier contact, the resistance of the

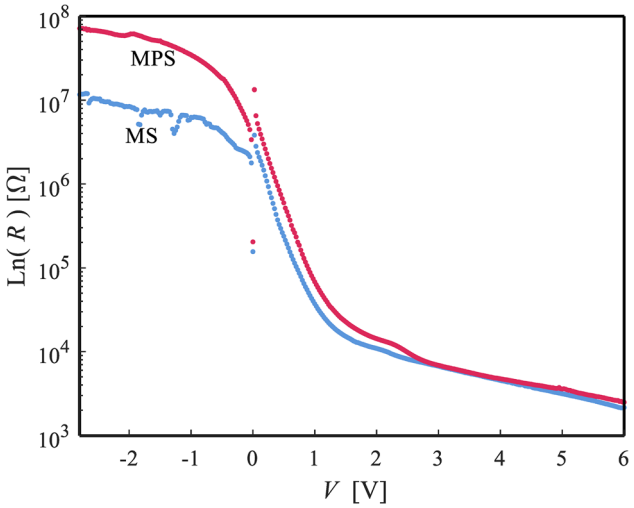

Fig. 5. The semi-logarithmic curves of the resistance of the MS and MPS SBDs.

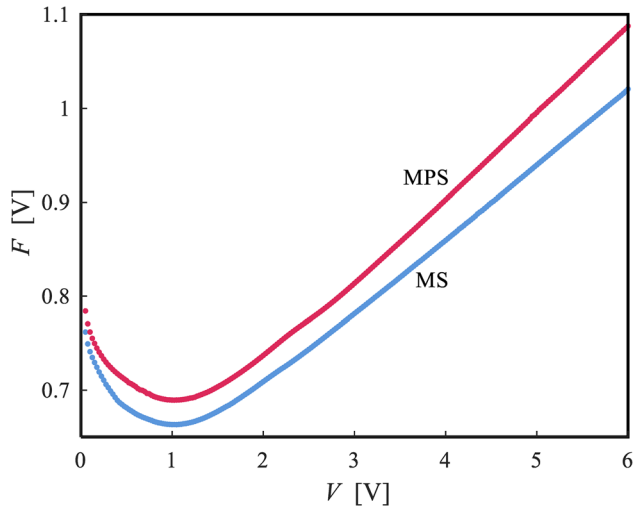

Fig. 6. The $F(V)$–V curves of the MS and MPS SBDs.

bulk of semiconductors, and no uniform doped atoms in the semiconductors.[49,50] Moreover, the R_{sh} value based on the physical defects such as holes in the bulk structures of crystals, high conductibility ways like grain boundaries or dislocations and also leakage current paths going through the interlayer between gate (front) and back contact or probe to the ground wire.[49,50]

The Fig. 5 shows that the R_i has a constant value and is independent of applied bias voltage both at the reverse and forward bias which matches to the real R_s and R_{sh} values, respectively. Hence, the R_s and R_{sh} values were calculated as 2.1 kΩ and 1.6 MΩ for MS and 2.5 kΩ and 66 MΩ for MPS structures, respectively. Consequently, in MPS diode the value of R_{sh} is closer to the ideal diode ($\geq 10^9$ Ω) compared with MS type SBD.

There are various methods to obtain R_s values. The nature of these methods may vary due to different voltage biases and measuring system.[49,52,56,57] On the other hand, the values of BH, ideality factor and R_s of the SBDs usually depend on applied bias voltage and the nature of measurement system or method. Therefore, the values of BH and R_s were also acquired by the Norde functions modified by Bohlin.[52,58] Especially, when the LnI–V curve does not have a distinctive linear region or a very narrow linear region, the accuracy and reliability of calculations are reduced. In this case, Norde developed a method to calculate the BH and R_s by using the curve of the function (for n = 1). Later, the Norde[52] method was modified by Bohlin[58] as follows:

$$F(V) = \frac{V}{\gamma} - \frac{kT}{q}\left[\ln\left(\frac{I(V)}{AA^{*}T^{2}}\right)\right]. \quad (5)$$

In Eq. 5, $\beta(= q/kT)$ is thermal energy, γ is the dimensionless quantity which is larger than n. Thus, $F(V)$ versus V curves for without interlayer and Ag_2S-PVA interlayered structures were extracted from Eq. 5 and presented in Fig. 6.

These curves for two types of SBDs pass a minimum point ($F(V_0)$). Concerning the Norde method, the valuation of R_s and Φ_{B0} can be acquired from the relations below:

$$R_s = \frac{kT(\gamma - n)}{qI_o}, \quad (6a)$$

$$\Phi_{B0} = F(V_o) + \frac{V_o}{\gamma} - \frac{kT}{q}, \quad (6b)$$

where V_0 and I_0 are the minimum points coordinates of the $F(V_0)$ in $F(V)$ versus V curve. Thus, by using Eqs. 6a and 6b, both the value of R_s and Φ_{B0} were found as 3.17 kΩ and 0.710 eV for MS and 5.28 kΩ and 0.806 eV for MPS type SBDs. Observations showed that both BH and R_s values acquired by using the Norde method are higher than TE theory/Ohm's Law for the two types of structures. These discrepancies of the BH depend upon applied bias voltage or the nature of the used calculation method.

In general, the valuation of the n and Φ_{B0} which was acquired from the intercept and slope of the linear part of Ln(I) versus V curves at forwarding bias region, are practically independent of the applied voltage. But after the linear region, they are mightily dependent on applied bias voltage as related to Eqs. 7a and 7b[51]: Therefore, while the value of R_s dominates in the downward of the I–V curve, N_{ss} dominates at the low and intermediate bias voltages. The profile of N_{ss} changes from region to region between interlayer and semiconductor in the bandgap. This distribution of N_{ss} with energy can be obtained by considering the voltage-dependent effective BH (Φ_e) which is contained in the n as follows.[51]

$$\Phi_e = \Phi_{Bo} + \alpha\,(V) = \Phi_{Bo} + \left(1 - \frac{1}{n(V)}\right)V, \qquad (7a)$$

$$n(V) = \frac{qV}{kT \cdot Ln\left(I/I_o\right)} = 1 + \frac{\delta}{\varepsilon_i}\left[\frac{\varepsilon_s}{W_D} + qN_{ss}(V)\right]. \qquad (7b)$$

In Eqs. 7a and 7b, $\alpha(V)$ (= $d\Phi_e/dV$) is the changing in the BH with applied biases, W_D is the depletion layer width which may be computed from the reverse bias C^{-2} versus V curve at higher frequencies, ε_s and ε_i are the permittivity of semiconductor material and interface layer, respectively. For the *n*-type semiconductor, the energy of surface states (E_{ss}) to conduction band edge (E_c) is expressed by[51]

$$E_c - E_{ss} = q(\Phi_e - V). \qquad (8a)$$

In the MIS or MPS structures, the surface states are completely governed by a semiconductor or in other words, the charges at surface states are in-equilibrium with semiconductor when the interfacial layer thickness is higher than 30 Å. Thus, the energy-dependent profile of N_{ss} is deduced by Card as follow[51]:

$$N_{ss}(V) = 1/q[\varepsilon_i/\delta(n(V) - 1) - \varepsilon_s/W_D], \qquad (8b)$$

where, δ is the interfacial layer thickness. Therefore, the N_{ss} density distribution profiles for both type SBDs were acquired from the forward bias *I*–*V* data by using Eqs. 8a and 8b and are given in Fig. 7.

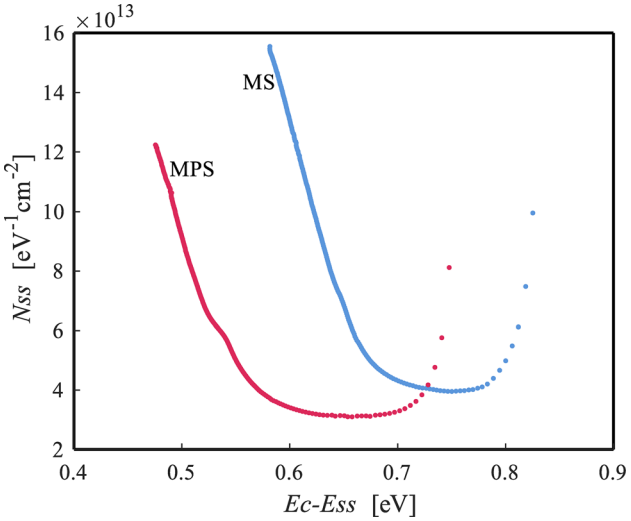

Fig. 7. The energy density distribution curves of the MS and MPS SBDs.

As shown in Fig. 7, for both SBDs, the N_{ss} versus (E_c–E_{ss}) have almost U shape behavior and this behavior indicates that the N_{ss} value increases from just about the forbidden band gap's center (E_g) of Si towards the conduction band's underside. The tail in Fig. 7 for N_{ss} is attributed to the surface states deep level density in the nearly forbidden bandgap of silicon. Figure 7 shows that from the conductivity band (E_c) to almost the middle of the forbidden band gap (E_g) the N_{ss} values of the MPS structure are lower than that of the MS structure and thereafter the N_{ss} values of these two structures approach each other. This is the consequence of particular density distribution of the N_{ss} and their re-order and re-structure under an applied bias voltage. The schematic energy band diagrams of the Au/*n*-Si (MS) and Au/(Ag_2S-PVA)/*n*-Si (MPS) diodes including the interface states, interface polymer layer and

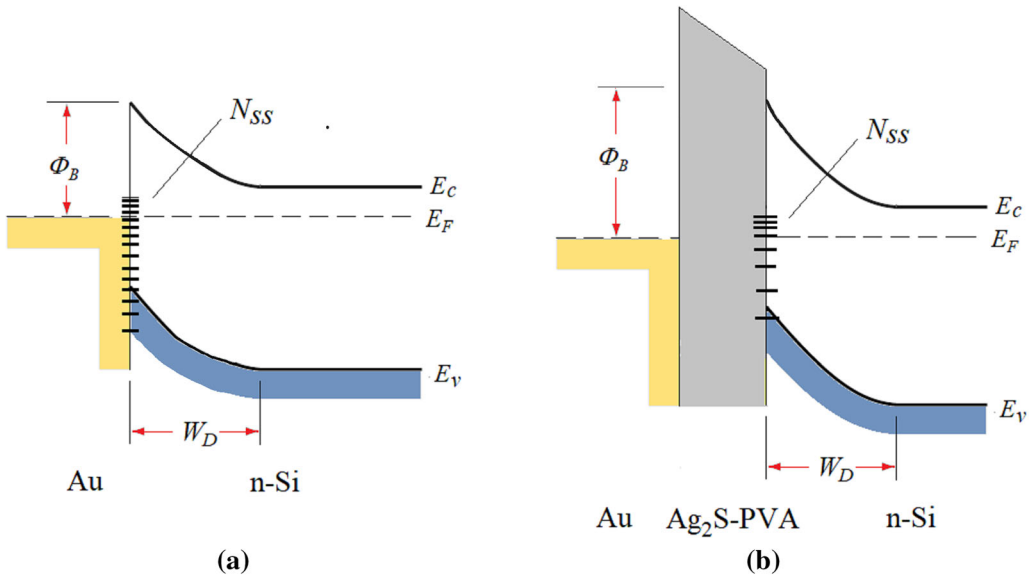

Fig. 8. Energy band diagram of (a) Au/*n*-Si (MS) and (b) Au/(Ag_2S-PVA)/*n*-Si (MPS) diode.

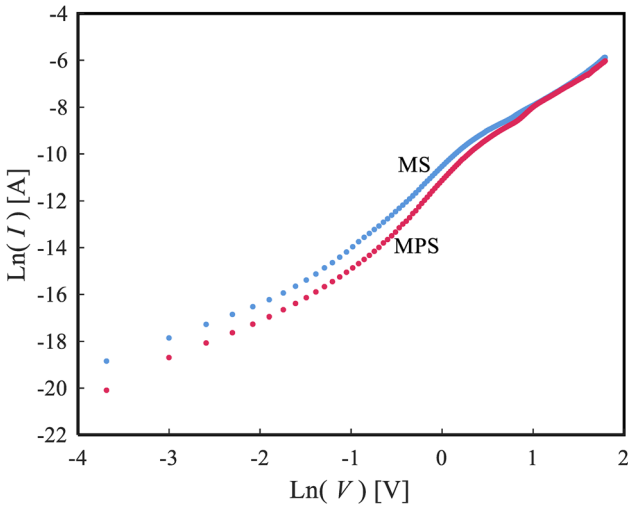

Fig. 9. The ln(*I*)–ln(*V*) curves of the MS and MPS SBDs.

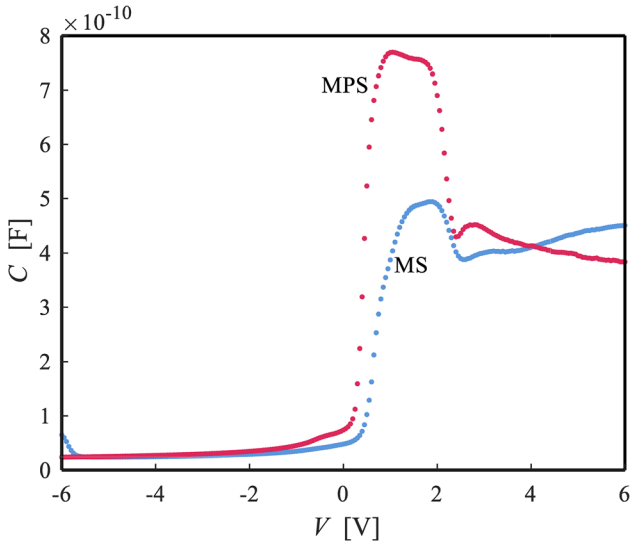

Fig. 10. The *C*–*V* curves of the MS and MPS SBDs.

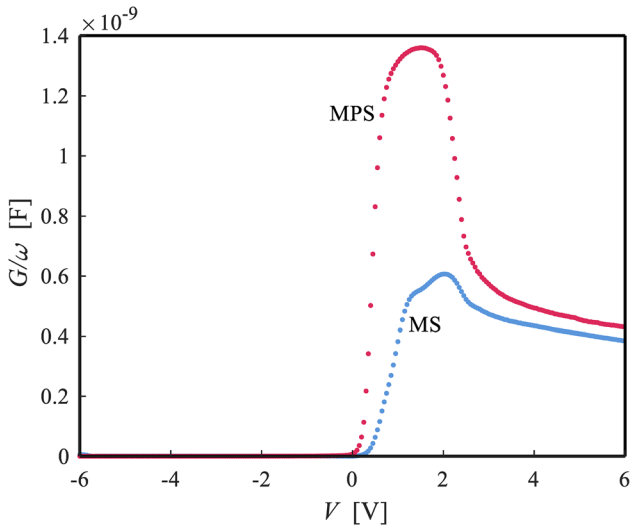

Fig. 11. The *G*/*ω*–*V* curves of the MS and MPS SBDs.

BH are shown in Fig. 8. This figure shows that the interface layer between metal and semiconductor provides the band bending that leads to an increase in BH. Moreover, such a polymer interfacial layer filling interface states (N_{ss}) or traps and, therefore, regulates electrical charge flows. These results confirm that the Ag_2S-PVA interface layer enhanced the performance of MS diode due to the increase of BH and decrease of the average N_{ss}.

To specify possible conduction mechanisms such as space charge limited current (SCLC), trap charge limited current (TCLC), and ohmic behavior; the Ln(*I*) versus Ln(*V*) curves were drawn and represented in Fig. 9. It is clear that these curves have three prominent linear areas with various slopes, correspond to low, intermediate and high forward bias voltages for both structures. This attitude of the Ln(*I*)–ln(*V*) curves display a power-law behavior of the current ($I \sim V^m$), where m is the slope of the curves. The values of slope of the Ln(*I*) versus Ln(*V*) curve for low, intermediate and high bias regions were found as 2.09, 3.44, and 2.40 for the MS type SBD and 1.75, 4.18, and 2.58 for the MPS type SBD. When these slopes are taken into account, the current conductions in the low bias display almost ohmic behavior for two types of structures due to the existence of the thermally generated carriers.[55] Both in the intermediate and higher bias voltages ($n > 2$), the current conduction is governed by TCLC. As for the TCLC, an increase in the injected charges number causes the N_{ss} or traps to be filled and an increase in the space charge.

Capacitance–Voltage (C–V) Characteristics

The *C*–*V* and G/ω-*V* data for all types of metal–semiconductor structures can be used to understand the origin of N_{ss}, which are in equilibrium with semiconductor and possible conduction mechanisms. Since these measurements are applied at enough high frequencies (≥ 0.5 MHz), the charge located N_{ss} cannot follow the ac signal.[57] The *C*–*V* and G/ω-*V* characteristics of the fabricated SBDs for 1 MHz are presented in Figs. 9 and 10 respectively.

In Figs. 10 and 11, the *C*–*V* and G/ω–*V* curves especially in depletion and accumulation regions have noticeable changes with the voltage due to the effects of surface states, interface layer and series resistances. While the surface states are the effectual factor in the depletion region, series resistances and interlayer are effectual factors at the accumulation region. Usually, *C*–*V* and G/ω-*V* curves indicate an increment with the rising voltage. In this case, both the *C*–*V* and G/ω-*V* curves give a peak at about 1.5 V. Such an anomalous peak can be attributed to the existence of R_s and particular density distribution of N_{ss} between the interlayer and semiconductor in the forbidden bandgap.[59,60]

The reverse bias of the C^{-2}–V curve is very important to analyze the experimental C–V data. Applying the C–V measurements at 1 MHz and higher frequencies, all types of structure's capacitance in the depletion region can be determined as [49];

$$C^{-2} = 2(V + V_0)/(q\varepsilon_s\varepsilon_0 A^2 N_D). \quad (9)$$

In Eq. 9, V_0 is the intercept voltage, which is extrapolated from the leaner part of the C^{-2}–V curves. Therefore, to assess the parameters such as V_D, Fermi energy level (E_F), N_D, W_D, and $\Phi_B(C$–$V)$ of the fabricated structures, the C^{-2}–V curves were drawn and are shown in Fig. 12. As shown in this figure, the C^{-2}–V curves as a function of reverse bias voltage have a good linear behavior that indicates the formation of SBDs. The value of the N_D was calculated using the slope of the C^{-2}–V curve for both structures. Consequently, the value of $\Phi_B(C$–$V)$, was determined as:

$$\Phi_B(C-V) = (V_o + kT/q) + kT/q\, Ln(N_c/N_d) = V_d + E_F \quad (10)$$

with

$$E_F = \ln(N_C/N_D)kT/q, \quad (11a)$$

$$N_C = 2[2\pi m_e * m_0 kT/h^2]^{1.5}. \quad (11b)$$

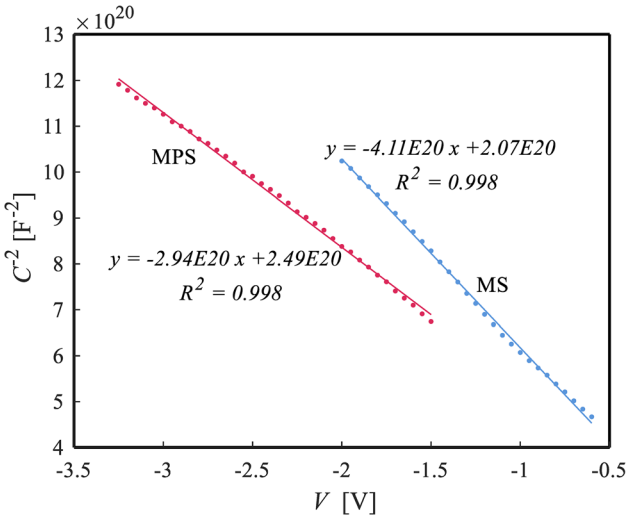

Fig. 12. The C^{-2}–V curves of the MS and MPS SBDs.

In Eq. 11a and 11b, N_C is the effective density of states in the conduction band of silicon, m_e^*(= 0.98 m_0) is the effective mass of the electron, and m_0 is rest mass of the electron, respectively. Thus, the value of E_F was readily calculated from Eq. 11a.[49–51] The results for the V_D, N_D, E_F, W_D, and $\Phi_B(C$–$V)$ for two types of SBDs are tabulated in Table I. The obtained experimental values of BH from the forward bias Ln(I)–V is lower than the reverse bias C^{-2} versus V characteristics due to the nature of measurement method and various bias voltage range. The other reason for the discrepancy in BH determined from I–V and C–V characteristics are the result of barrier inhomogeneity and a special energy density distribution between metal and semiconductors. In other words, the current flows through the lower barriers at about a mean value of BH in the forward biases. Contrarily, the electronic charges distribution at the depletion region affect the BH values determined from reverse biases C–V characteristics and these charges distribution complies with the weighted arithmetic mean of the barrier inhomogeneity.[55] On the other hand, Song et al.[61] reported that, this discrepancy in the BH specified from forwarding biases I–V and reverse biases C–V characteristics are the result of interface layer composition, its non-homogeneity and the distribution of surface charges.

All experimental results indicate that the use of (Ag_2S-PVA) organic interfacial layer at Au/n-Si interface leads to an increase in the performance of Au/n-Si (MS) structure such as causes a distinctive reduction in the leakage current, surface states, R_s and increase in BH which were obtained from both forward bias I–V and reverse bias C^{-2}–V characteristics. These results are evidence of the increased performance of the MS type SBD due to the effect of the organic interfacial layer. In other words, (Ag_2S doped-PVA) organic interlayer can be utilized successfully instead of conventional insulator or oxide layer due to easily grown processes, low cost, low weight, low energy requirement, and flexibility of them. Experimental results show that the MPS structure's rectifying ratio is 38 times greater than the MS structure. Additionally, the N_{ss} value of the MPS structure at near mid-gap of Si is lower than the MS structure at about 10 times. These results also confirmed that (Ag_2S-PVA) organic interfacial layer improved the MS structure's performance due to the passivation effect of the interfacial organic layer. Because, conjoining Ag_2S in PVA lattices decreases the oxygen vacancies

Table I. The calculated V_0, E_F, N_D, Φ_B, and W_D values from the C–V data of the MS and MPS SBDs

Structure	$V_0 = V_i$ (V)	E_F (eV)	N_D (cm^{-3})	Φ_B (eV)	W_D (cm)
Au/n-Si	0.507	0.309	5.84×10^{13}	0.842	2.18×10^{-05}
Au/Ag2S/n-Si	0.321	0.289	1.29×10^{14}	0.736	1.74×10^{-05}

and causes effects to charge carriers at lower densities, which can effectively enlarge the barrier height at the metal–semiconductor interface.

CONCLUSION

The preparation of Au/*n*-Si (MS) SBDs with and without (Ag_2S-PVA) interlayer were made by the aid of the ultrasound-assisted method. Their structural, optical, morphological and electrical characteristics were obtained via x-ray diffraction (XRD), scanning electron microscopy (SEM), UV–Visible spectroscopy and finally *I–V* and *C–V* measuring devices. The XRD result proved the existence of α-phase in the Ag_2S nanostructure, UV–Visible spectrum proves the quantum confinement of Ag_2S nanostructure, and SEM image shows the grain size of the Ag_2S in nanoscale. The ideality factor (n) and barrier height (BH) at zero bias ($\Phi_{B0}(I–V)$) were obtained from the *I–V* data. Thus, the values of I_0, n, and Φ_{B0} were found as 1.17×10^{-7} A, 6.78, and 0.74 eV for the MS and 3.62×10^{-8} A, 6.17, and 0.77 eV for the MPS structure, respectively. Here, the results confirmed the utilized (Ag_2S-PVA) interface layer causes MS type SBD performance to increase. Other important electrical parameters that directly indicate the performance of the SBDs are the series and shunt resistance. In this case, the shunt and series resistances values were calculated as 1.6 MΩ and 2.1 kΩ for MS and 66 MΩ and 2.5 kΩ for MPS structure, respectively. Consequently, in the MPS diode the value of R_{sh} is closer to the ideal diode ($\geq 10^9$ Ω) in comparison with MS diode. Furthermore, it has been found that from the conductivity band (E_c) to almost the middle of the forbidden bandgap (E_g) the N_{ss} values of the MPS structure are lower than that of the MS structure and thereafter the N_{ss} values of these two structures approach each other. Generally, it can be said that the (Ag_2S-PVA) interlayer enhanced the performance of the diode considerably in terms of high rectifier rate (RR), shunt resistance (R_{sh}), and low N_{ss} and R_s. Thus, the (Ag_2S-PVA) interlayer can be used in a MS type diode instead of the other insulator layer.

REFERENCES

1. R. Goyal, *Nanomaterials and Nanocomposites* (Boca Raton: CRC Press, 2018).
2. P. Biehl, M. vonder Lühe, S. Dutz, and F.H. Schacher, *Polymers* 10, 1 (2018).
3. T. Jin, Q. Han, Y. Wang, and L. Jiao, *Small* 14, 1703086 (2018).
4. B. Ajitha, Y.A. Kumar Reddy, and P. Sreedhara Reddy, *Powd. Technol.* 269, 110 (2015).
5. G. Anandha Babu, G. Ravi, Y. Hayakawa, and M. Kumaresavanji, *J. Magn. Magn. Mater.* 375, 184 (2015).
6. T. Ali and A. Venkataraman, *Int. J. Adv. Eng. Technol.* 7, 122 (2014).
7. Y. Azizian-Kalandaragh, F. Sedaghatdoust-Bodagh, and A. Habibi-Yangjeh, *Superlatt. Microstruct.* 81, 150 (2015).
8. K.T. Al-Rasoul, I.M. Ibrahim, M. Ali, and R.M. Al-Haddad, *Int. J. Sci. Technol. Res.* 3, 213 (2014).
9. P. Saha, T.P. Majumder, and S.C. Debnath, *Int. J. Eng. Sci. Innov. Technol.* 3, 86 (2014).
10. Y. Azizian-Kalandaragh, *Optoelectron. Adv. Mater.-Raped Commun.* 10, 201 (2016).
11. S. Boughdachi, Y. Azizian-Kalandaragh, Y. Badali, and Ş. Altındal, *J. Mater. Sci.: Mater. Electron.* 28, 17948 (2017).
12. Y. Azizian-Kalandaragh, F. Sedaghatdoust-Bodagh, E. Alizadeh-Gheshlaghi, and A. Khodayari, *J. Nanoelectron. Optoelectron.* 12, 1 (2017).
13. U.M. Jadhav, S.N. Patel, and R.S. Patil, *Res. J. Chem. Sci.* 3, 69 (2013).
14. H. Dlala, M. Amlouk, S. Belgacem, P. Girard, and D. Barjon, *Eur. Phys. J.* 2, 13 (1998).
15. T.G. Schaaff and A.J. Rodinone, *J. Phys. Chem. B.* 107, 10416 (2003).
16. N. Belman, Y. Golan, and A. Berman, *Cryst. Growth Des.* 5, 439 (2005).
17. A.P. Yadav and R.R. Pradhananga, *J. Nepal Chem. Soc.* 15, 19 (1996).
18. W. Lou, X. Wang, M. Chen, W. Liu, and J. Hao, *Nanotechnology* 19, 225607 (2008).
19. R.G. Cope and H.J. Oldsmid, *Br. J. Appl. Phys.* 16, 501 (1965).
20. R. Zamiri, H. Abbastabar Ahangar, A. Zakaria, G. Zamiri, M. Shabani, B. Singh, and J.M.F. Ferreira, *Chem. Cent. J.* 9, 28 (2015).
21. A.K. Abass, *Solar Energy Mater.* 17, 375 (1988).
22. J. Joo, H.B. Na, T. Yu, J.H. Yu, Y.W. Kim, F. Wu, J.Z. Zhang, and T. Hyeon, *J. Am. Chem. Soc.* 12, 11100 (2003).
23. D. Qin, L. Zhang, G. He, and Q. Zhang, *Mater. Res. Bull.* 48, 3644 (2013).
24. L. Wang, M. Lu, X. Wang, Y. Yu, X. Zhao, P. Lv, H. Song, X. Zhang, L. Luo, C. Wu, Y. Zhang, and J. Jie, *J. Mater. Chem. A.* 1, 1148 (2013).
25. Z. Yu-ming, Z. Yi-men, P. Alexandrov, and J.H. Zhao, *Chin. J. Semicond.* 22, 265 (2001).
26. D. Korucu and A. Turut, *Int. J. Electron.* 101, 1595 (2014).
27. Z. Haiyan, Y. Zhizhen, H. Jingyun, L. Bei, X. Jinghong, and Z. Binghui, *Chin. J. Semicond.* 24, 622 (2003).
28. I. Mukherjee, S. Senapati, D. Mitra, A.K. Ras, S.P. Das, and S.P. Moulik, *J. Colloids Surf. A: Physicochem. Eng. Asp.* 360, 142 (2010).
29. M. Chen, Y. Xie, H.Y. Chen, Z.P. Qiao, and Y.T. Qian, *J. Colloid Interf. Sci.* 47, 237 (2001).
30. M. Liu, Z. Xu, B. Li, C. Lin, D. Bai, N. Shan, and W. You, *Mater. Lett.* 65, 555 (2011).
31. H.M. Pathan, P.V. Salunke, B.R. Sankpal, and C.D. Lokhande, *Mater. Chem. Phys.* 72, 105 (2011).
32. H. Nozaki, M. Onoda, K. Yukino, K. Kurashima, K. Kosuda, H. Maki, and S. Hishita, *J. Solid State Chem.* 177, 1165 (2004).
33. M. Chen and L. Gao, *Mater. Letter.* 60, 1059 (2006).
34. S.S. Dhumure and C.D. Lokhande, *Thin Solid Films* 1, 240 (1994).
35. M.M. El-Nahass, A.A.M. Farag, E.M. Ibrahim, and S. Abdel-Rahman, *Vacuum* 72, 453 (2004).
36. W. Yang, L. Zhang, Y. Hu, Y. Zhong, H. BinWu, and X.W. Lou, *Angew. Chem. Int. Ed.* 51, 11501 (2012).
37. M. Kristl, S. Gyergyek, and J. Kristl, *Mater. Express.* 5, 359 (2015).
38. X. Wen, S. Wang, Y. Xie, X.-Y. Li, and S. Yang, *J. Phys. Chem. B.* 109, 10100 (2005).
39. V.G. Debabov, T.A. Voeikova, A.S. Shebanova, K.V. Shaitan, L.K. Emelyanova, L.M. Novikovaa, and M.P. Kirpichnikov, *Nanotechnol. Russ.* 8, 269 (2013).
40. J.P. Xiao, Y. Xie, R. Tang, and W. Luo, *J. Mater. Chem.* 12, 1148 (2002).
41. J.H. Bang and K.S. Suslick, *Adv. Mater.* 22, 1039 (2010).
42. M.I. Díez-García, V. Manzi-Orezzoli, M. Jankulovska, S. Anandan, P. Bonete, R. Gómez, and T. Lana-Villarreal, *Phys. Procedia* 63, 85 (2015).
43. A. Buyukbaşş Uluşan, S. Altındal Yerişkin, A. Tataroğlu, M. Balbaşi, and Y. Azizian, *J. Mater. Sci.: Mater. Electron.* 29, 8234 (2018).

44. N. Baraz, I. Yücedağ, Y. Azizian-Kalandaragh, and Ş. Altındal, *J. Mater. Sci.: Mater. Electron.* 29, 12735 (2018).
45. E.E. Tanrıkulu, Ş. Altındal, and Y. Azizian-Kalandaragh, *J. Mater. Sci.: Mater. Electron.* 29, 11801 (2018).
46. Ç. Bilkan, Y. Badali, S. Fotouhi-Shablou, Y. Azizian-Kalandaragh, and Ş. Altındal, *Appl. Phys. A* 123, 560 (2017).
47. H.P. Klug and L.E. Alexander, *X-ray Diffraction Procedures*, 2nd ed. (NewYork: Wiley, 1964).
48. E.A. Akhlaghi, Y. Badali, S. Altindal, and Y. Azizian-Kalandaragh, *Physica B-Condens. Matter.* 546, 93 (2018).
49. S.M. Sze, *Physics of Semiconductor Devices*, 3rd ed. (New York: Wiley, 1981).
50. E.H. Rhoderick, *Metal-Semiconductor Contacts* (London: Oxford University, 1978).
51. H.C. Card and E.H. Rhoderick, *J. Phys. D Appl. Phys.* 4, 1589 (1971).
52. H.J. Norde, *J. Appl. Phys.* 50, 5052 (1979).
53. S. Altındal Yerişkin, M. Balbaşı, and İ. Orak, *J. Mater. Sci.: Mater. Electron.* 28, 14040 (2017).
54. Y. Badali, A. Nikravan, S. Altindal, and I. Uslu, *J. Electron. Mater.* 47, 3510 (2018).
55. V.R. Reddy, *Thin Solid Film.* 556, 300 (2014).
56. S.K. Cheung and N.W. Cheung, *Appl. Phys. Lett.* 49, 85 (1986).
57. E.H. Nicollian, *Mos (Metal Oxide Semiconductor) Physics and Technology* (Hoboken: Wiley, 2002).
58. K.E. Bohlin, *J. Appl. Phys.* 60, 1223 (1986).
59. Ş. Altındal and H. Uslu, *J. Appl. Phys.* 109, 074503 (2011).
60. E.E. Tanrıkulu, S. Demirezen, Ş. Altındal, and İ. Uslu, *J. Mater. Sci.: Mater. Electron.* 29, 2890 (2018).
61. V.R. Reddy, V. Manjunath, V. Janardhanam, Y. Kil, and C.J. Choi, *J. Electron. Mater.* 43, 3499 (2014).